

Quantum Noise Spectroscopy of Nanoscale Charge Defects in Silicon Carbide at Room Temperature

Jinpeng Liu,^{1,2,3,*} Yuanhong Teng,^{2,*} Yu Chen,^{2,4,*} Yixuan Wang,^{2,4} Chihang Luo,² Jun Yin,^{1,2,3} Hao Li,⁵ Lixing You,⁵ Ya Wang,^{2,4,6} Qi Zhang,^{1,3,7,†} and Fazhan Shi^{1,2,3,4,6,‡}

¹*School of Biomedical Engineering, Division of Life Sciences and Medicine, University of Science and Technology of China, Hefei, Anhui, 230026, P.R.China*

²*Laboratory of Spin Magnetic Resonance, School of Physical Sciences, Anhui Province Key Laboratory of Scientific Instrument Development and Application, University of Science and Technology of China, Hefei 230026, China*

³*Suzhou Institute for Advanced Research, University of Science and Technology of China, Suzhou, Jiangsu, 215123, P.R.China*

⁴*Hefei National Laboratory, University of Science and Technology of China, Hefei 230088, China*

⁵*Shanghai Key Laboratory of Superconductor Integrated Circuit Technology, Shanghai Institute of Microsystem and Information Technology, Chinese Academy of Sciences, Shanghai 200050, China*

⁶*Hefei National Research Center for Physical Sciences at the Microscale, University of Science and Technology of China, Hefei 230026, China*

⁷*Institute of Quantum Sensing, School of Physics, Institute of Fundamental and Transdisciplinary Research, Zhejiang Key Laboratory of R&D and Application of Cutting-edge Scientific Instruments, Zhejiang University, Hangzhou, 310027, China*

The nanoscale charge environment critically influences semiconductor physics and device performance. While conventional bulk characterization techniques provide volume-averaged defect properties, they lack the spatial resolution to resolve nanoscale charge heterogeneity and identify microscopic noise sources. Here, we utilize single PL5 centers in 4H-SiC as room-temperature broadband quantum sensors to fill in the gap. We report the first real-time, nanoscale observation of single-charge tunneling dynamics in a commercial semiconductor at room temperature, by monitoring the random telegraph noise using optically detected magnetic resonance (ODMR). This capability enables an electrical noise imaging technique, showing distinct noise variations across different wafer substrates. By employing dynamical decoupling, we extend noise spectroscopy from near-DC to MHz frequencies, uncovering significant noise spectral density correlations across frequency bands. Finally, we probe MHz-GHz noise and identify its origin via T_1 relaxation spectroscopy, obtaining the first nanoscale electron paramagnetic resonance (EPR) spectroscopic fingerprint of charge defects in SiC. These techniques open avenues for characterizing noise environments in semiconductor devices, providing critical insights for optimizing SiC fabrication processes, defect control, and advancing quantum technologies.

Silicon carbide is recognized as a promising semiconductor material due to its outstanding physical properties, such as high thermal conductivity and wide band gap, making it ideal for the fabrication of high-power devices [1]. However, the performance and reliability of SiC-based complementary metal-oxide-semiconductor (CMOS) devices are fundamentally limited by atomic-scale defects in bulk and interface, which act as noise sources, reduce carrier lifetimes, and trigger breakdown [2]. Despite the maturity of SiC fabrication, characterizing the microscopic electric and magnetic environments associated with these defects presents a critical challenge. Conventional methods like standard deep level transient spectroscopy (DLTS), electron spin resonance (ESR) and macroscopic photoluminescence (PL) yield only volume-averaged metrics [3], inherently preventing the identification and localization of noise sources at the nanoscale.

To fill this gap, solid-state quantum sensors have emerged as promising tools for nanoscale diagnostics. While nitrogen-vacancy (NV) centers in diamond are widely employed for nanoscale electric field sensing [4–

13], their application to SiC is constrained by the sensor-sample distance and the inability to probe the intrinsic bulk environment of the semiconductor [14–16]. Moreover, single-charge tunneling events detected via photoluminescence excitation predominantly required cryogenic temperatures, thereby limiting their applicability to in-fab-line monitoring [10, 17–19]. To achieve true in-situ monitoring, we focus on utilizing intrinsic point defects within the 4H-SiC lattice itself. Among these, the PL5 and PL6 centers stand out not only for its optical addressability and spin coherence [20–23] but, more importantly, for its giant Stark effect. The Stark-coupling parameters of PL5 center are 2–7 times stronger than those of NV centers in diamond [24], making it into an ultra-sensitive electrometer capable of detecting local electric field fluctuations. This unique property makes PL5 center an ideal candidate for imaging the noise landscape inside SiC devices at room temperature.

Concurrently, recent research on solid-state spin qubits has revealed that, in addition to the magnetic spin bath, charge defects within the lattice constitute a primary

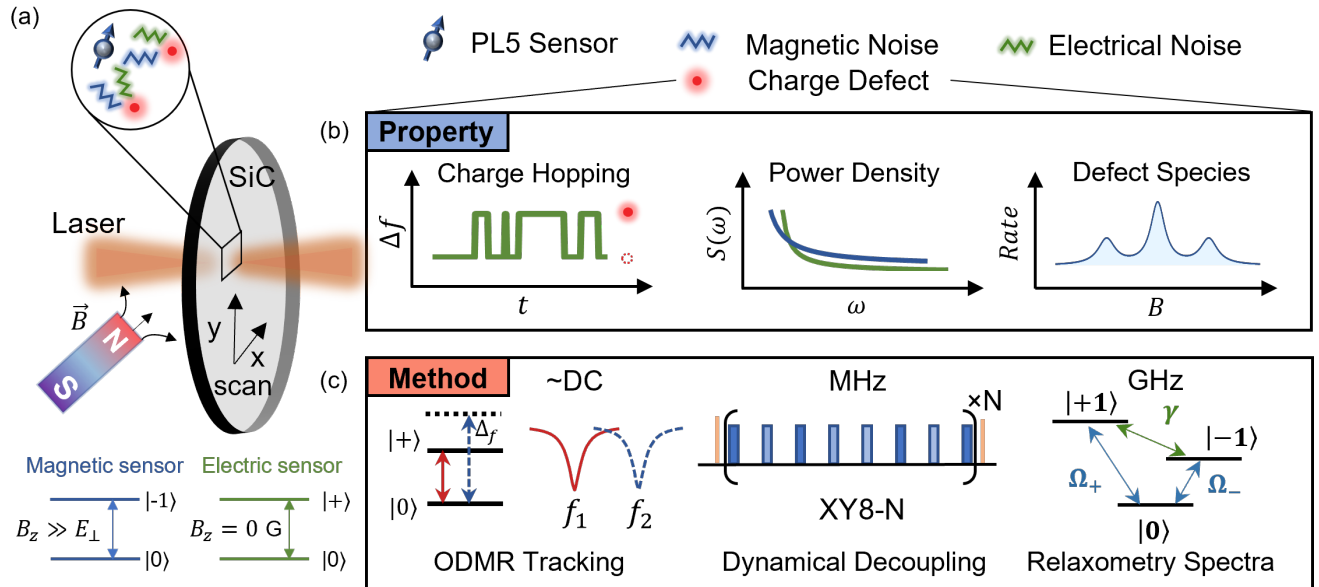


Fig.1. Experimental setup and sensing scheme overview. (a) Experiment principle of quantum sensor in silicon carbide. A 905nm laser is used to realize the initialization and readout of PL5 center. Electrical and magnetic noise in semiconductors can have a significant impact on the performance of high-power electronic devices as well as on the coherence properties of qubits embedded in solid-state materials. An external magnetic field parallel to the principal axis of PL5 center is applied to tune the energy levels when needed. The intrinsic non-zero term E_{\perp} for PL5 makes the transition between ground states $\{|0\rangle, |+\rangle\}$ exclusively sensitive to transverse electric noise under zero magnetic field. When B_z is applied, the transition becomes sensitive to longitudinal magnetic noise. (b) Physical properties of the local charge environment. The panels illustrate three key dimensions of defect characterization: (Left) Charge hopping, showing the time-domain random telegraph noise induced by discrete charge trapping and releasing events; (Middle) Power Density, displaying the frequency-domain noise spectrum for both magnetic (blue) and electrical (green) noise components; and (Right) Defect Species, revealing the spectroscopic fingerprint used to identify specific defects. (c) Corresponding quantum sensing protocols. The methods span from DC to GHz frequencies: (Left) Real-time tracking of ODMR resonance shifts Δf monitor low-frequency fluctuations; (Middle) Dynamical decoupling sequences (e.g., XY8) with variable inter-pulse spacing to probe noise power density in the MHz regime; and (Right) T_1 relaxometry spectra to probe charge defects species in the GHz regime.

source of decoherence [17, 25]. While existing studies have largely focused on monitoring and spatially localizing charge fluctuations in the DC-MHz regime at cryogenic temperatures [19], or suppressing noise via electric field depletion control [17, 25, 26], a method for the spectroscopic identification of nanoscale charge noise remains unrealized. This gap hinders the optimization of material growth and device fabrication processes for quantum technologies. Common semiconductor defects typically exhibit EPR spectra, making conventional ensemble-level EPR a vital tool for wafer inspection. Here, we advance EPR spectroscopic resolution to the nanoscale. By utilizing single PL5 centers as quantum sensors, we achieve real-time tracking of single-charge fluctuations and simultaneously characterize electric and magnetic noise across a broadband frequency range (from DC to GHz). This allows us to obtain the first nanoscale EPR spectroscopic fingerprint of charge defects in the immediate vicinity of the qubit. Crucially, we validated this method as a robust metrology tool by comparative noise imaging of commercial 4H-SiC wafers, observing distinct noise signatures that reveal intrinsic variations in substrate quality. These findings not only reveal the microscopic sources of electrical noise in quantum platforms built on solid-state qubits, but also introduce a powerful, non-invasive method for refining fabrication procedures in the

semiconductor industry.

Experimental setup and Sensing Scheme. A full landscape of our broadband noise detection technique routine in silicon carbide at room temperature is shown in Figure 1. Our sample was diced from a wafer consisting of an intrinsic epitaxial layer of single-crystal 4H-SiC grown on a 4° off-axis N-type 4H-SiC substrate. To generate PL5 centers, 60-keV $^{14}\text{N}^+$ ions were implanted at a dose of 10^{10} cm^{-2} followed by annealing for 30 minutes. More details are provided in Supplementary Material [27]. With this ion-implantation energy which corresponds to a penetration depth of 100 nm estimated by SRIM simulations [28], the majority of the generated sensors are embedded deep within the bulk, whose properties are governed by the intrinsic local environment rather than by surface conditions. A 905 nm laser is used to initialize and read the spin state of a single PL5 quantum sensor in 4H silicon carbide, where a fluorescence rate of 250 kcps (kilo counts per second) for a single PL5 center has been observed without photonic structure enhancement. The Hamiltonian of PL5 center is given by

$$H/\hbar = \frac{1}{\hbar^2} \left(D \hat{S}_z^2 - E_x (S_x^2 - S_y^2) + \gamma \mathbf{B} \cdot \mathbf{S} \right) \quad (1)$$

where $D \approx 1360 \text{ MHz}$ and $E_x \approx 16 \text{ MHz}$ (the coordinate is chosen to parallel the c-axis to the xz plane) [22, 23].

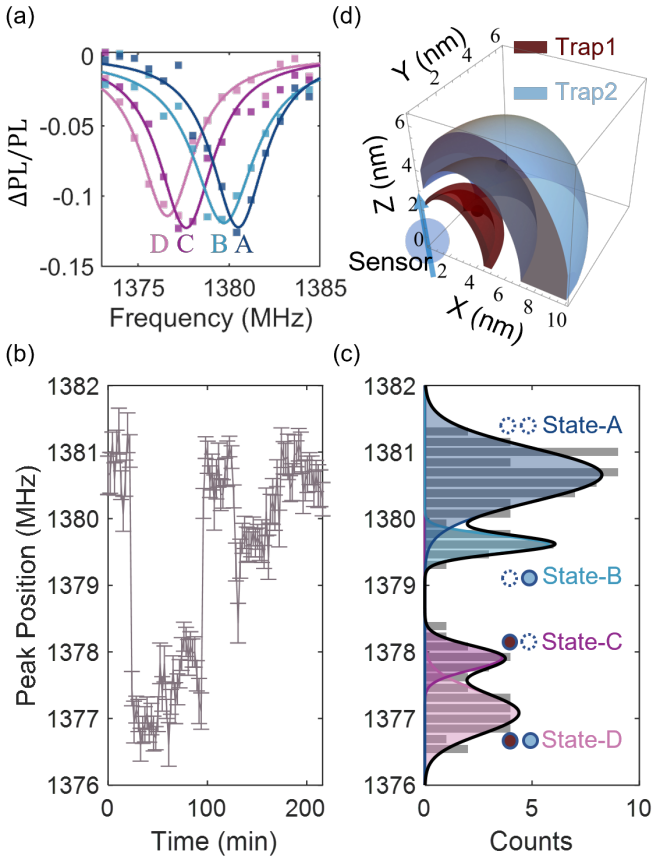


Fig.2. Nanoscale monitoring of electric environment at single charge level. (a) Four typical CW spectra configurations with different central frequency of a single quantum sensor were observed, which were labeled as A-D. (b) Time-resolved CW-ODMR measurements on a single PL5 center reveal the evolution of its spectral peak position. (c) Histogram illustrates the distribution of peak positions in (b). Four well-defined stable states can be clearly identified by fitting, corresponding to the four states identified in panel (a). The peak separation between State-A and C (B and D) is 3 ± 0.3 MHz, while that between State-A and B (C and D) is 1 ± 0.3 MHz. This indicates that the observed spectral fluctuations result from a composition of two two-level system (TLS) signals. (d) The possible location of the two charge traps with 95 % confidence interval based on the splitting of different states shown in (c). The detail of the calculation can be found in [27].

The Hamiltonian dictates that under zero magnetic field, the none-zero term E_x makes the transition between ground states exclusively sensitive to transverse electric noise. Microwave pulses are applied to coherently manipulate the spin. An external magnetic field parallel to the principal axis of PL5 center (labeled as B_z) is applied to tune the energy levels when needed. As illustrated in Figure 1(b-c), we employ a suite of coherent control sequences—ranging from continuous-wave (CW) monitoring to dynamical decoupling and T_1 relaxometry—to filter and track spectral fluctuations across a wide frequency bandwidth (DC to GHz). This setup effectively converts the PL5 center into a localized broadband spectrum analyzer for the surrounding electrical and magnetic environment induced by charge defects.

Single-Charge Dynamics. The change of local electric field will cause Stark shift between $|0\rangle$ and $|+\rangle / |-\rangle$ transitions as displayed in Figure 1(c), where $|+\rangle / |-\rangle = \frac{1}{\sqrt{2}}(|+1\rangle \pm | -1\rangle)$. Due to the orientation of the microwave field, spin manipulation between the $|0\rangle$ and $|+\rangle$ is more effective under zero magnetic field in our setup. For certain PL5 centers, we observed time-dependent spectral drift in their CW-ODMR results as shown in Figure 2. Figure 2(a) presents four representative ODMR spectral configurations (labeled State A to State D) acquired from the same individual color center. The raw data and their corresponding Lorentzian fits clearly show that the sensor exhibits distinct line shapes with shifted central frequencies at different moments, indicating a dynamic local environment. To systematically capture these dynamics, we performed a continuous spectral tracking measurement over a duration of several hours. The resulting time-resolved map, shown in Figure 2(b), visualizes the temporal evolution of the peak positions. By compiling the resonance frequencies extracted from this long-term trace, we obtained the statistical distribution presented in Figure 2(c). We attribute this behavior to the surrounding traps, which cause fluctuation of electric field when they capture or release charges. Based on the spectral splitting between different states (3 ± 0.3 MHz between state A and C, 1 ± 0.3 MHz between state C and D), we estimated the spatial position of the charge traps with 95 % confidence interval using the Stark shift coefficients of PL5 centers. Given the significantly larger transverse Stark coefficient compared to its longitudinal part ($d_{\perp} = 32.5$, $d_{\parallel} < 3$ Hz cm/V) [24], we infer that the observed electric field fluctuation originates from charge trapping and releasing events of two traps within a region of less than 10 nm [Figure 2(d)]. More analysis is shown in Supplementary Material [27].

Noise Imaging and Material Characterization
To evaluate the applicability of our method for material characterization, we investigated two distinct 4H-SiC epitaxial wafers (Wafer 1 and Wafer 2) obtained from different commercial manufacturers. Both samples were processed using identical ion implantation and annealing protocols to generate the PL5 center probes (details in Supplementary Material [27]). Despite sharing the same ion implantation fabrication history, the sensors exhibited strikingly different noise environments. While wafer 1 showed widespread spectral diffusion and instability [Figure 3(a)], wafer 2 demonstrated high spectral stability with minimal electrical noise [Figure 3(c)]. This pronounced contrast proves that our method is sufficiently sensitive to reveal the intrinsic differences in defect density and material quality between the starting substrates. By correlating the spatial locations of individual sensors with their measured noise levels, quantified by the standard deviation of the ODMR peak positions (σ_f), we constructed electrical noise maps for both samples [Figure 3(b,d)]. The noise map of Wafer

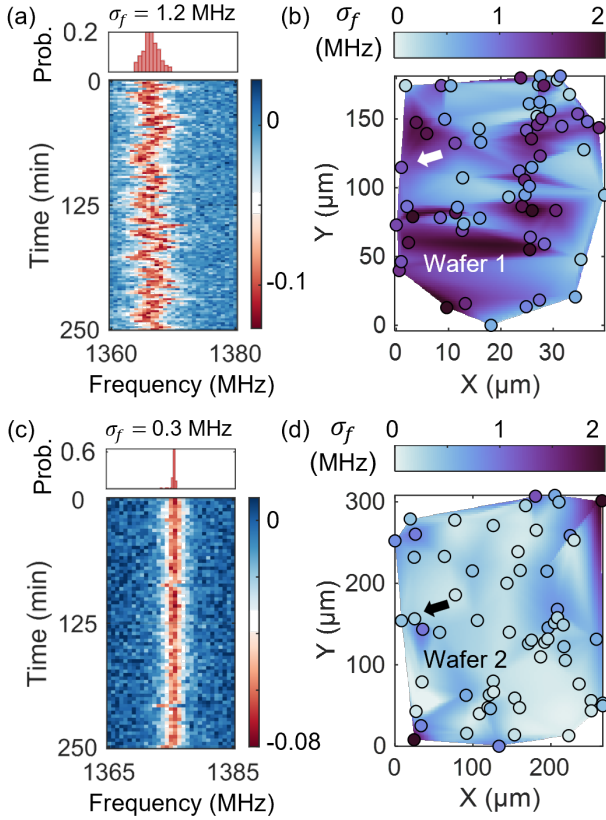


Fig.3. Electrical noise imaging of samples with different wafers. (a-b) CW-ODMR tracking data of a single PL5 center in sample from wafer 1. Standard deviation of the ODMR peak position σ_f is used to quantify the instability and the effective amplitude of ambient electrical noise. Right panel shows noise strength (σ_f) spatial distribution obtained by two-dimensional interpolation. (c-d) Same analysis in sample from wafer 2, which was diced from another manufacturer. Both wafers feature intrinsic epitaxial layers grown on n-type substrates.

1 reveals macroscopic spatial variations in noise density over tens of microns. This demonstrates the potential of our method as a powerful characterization tool for imaging the nanoscale electric noise distribution with single-charge-level sensitivity.

Noise Spectrum and Identification Having visualized the spatial heterogeneity of the electric noise, we carried out a detailed study on Sample 1 in subsequent experiments. We sought to identify its microscopic origin and explore the correlation in frequency domain. First, we measured the Hahn echo coherence time T_2 of 8 sensors and two different PL5 centers (designated PL5-A and PL5-B) exhibiting different CW-ODMR stability ($\sigma_{fA} = 0.18$ MHz; $\sigma_{fB} = 0.86$ MHz) were selected for detailed investigation. Note that here we use the two-point measurement method to enhance the temporal resolution [27, 29, 30]. As shown in Figure 4(a), the unstable sensor PL5-B exhibits a pronounced reduction in T_2 by up to an order of magnitude compared to the stable sensor PL5-A. To more clearly reveal this correlation, we plotted σ_f of the 8 sensors against their Hahn

echo coherence times as shown in Figure 4(b). A clear correlation is observed, indicating a rapid decrease of coherence as σ_f increases. The dashed line is fitted with $T_2 \propto 1/\sigma^k$ ($k \approx 0.8$), under the assumption of a universal noise spectral density across the sample. However, for the three PL5 centers with the largest values of σ_f , the measured coherence times fall below the fitted trend. These experimental deviations suggest that the local defect environments around these PL5 centers may exhibit distinct dynamical behaviors. To further investigate the noise spectra of PL5 A and B at higher frequencies up to MHz, we implemented XY8-1 dynamical decoupling protocols on the two PL5 under zero-field and axial magnetic field (~ 120 G). At zero magnetic field, longitudinal magnetic noise is suppressed by the transverse strain field E_x , so decoherence is governed by electric noise along x direction. In contrast, under $B_z > 100$ G, the transverse electromagnetic fluctuations are suppressed, and because the Stark coefficient for the longitudinal electric response of PL5 center is exceptionally small—longitudinal magnetic noise becomes the dominant source of decoherence [31, 32] as mentioned in Fig. 1(a). Under the delta-function filter approximation, we obtained the noise spectrum as shown in Figure 4(c). The results indicate a difference in the noise environments of the two sensors. For the spectrally stable PL5-A at near-DC range (with lower σ_f), the electric noise spectrum also stays at a low level in the sub-MHz range, implying that its magnetic noise is predominantly caused by the surrounding spin bath. In contrast, PL5-B exhibits significantly higher electric noise, accompanied by a magnetic noise intensity several times greater than that of PL5-A. This suggests that, beyond the intrinsic spin bath, the magnetic noise of PL5-B is strongly influenced by electromagnetic induction arising from proximal charge fluctuations. These findings confirm that minimizing the proximity effect of electromagnetic noise through fundamental charge engineering is a critical step to realizing high-coherence quantum sensors [17, 25]. More results of higher order dynamical decoupling are provided in the Supplementary Materials [27].

To extend our noise-spectroscopy window from the MHz to GHz regime, we applied a magnetic field along the PL5 center axis and scanned the B_z to tune the PL5 centers energy levels and subsequently performed T_1 relaxation measurement. By measuring the evolution curves under different initialization and readout conditions $S_1 \sim S_4$ as shown in [Figure 4(d)], we extracted the single-quantum (SQ) and double-quantum (DQ) transition rates, denoted as Ω_+/Ω_- and γ as shown in Figure 4(e) (inset figure) [31], which represent the magnetic and electric noise strength in our system. After preparing the initial state of PL5 center at the eigenstates $m_s = 0, \pm 1$ by laser and microwave pulses ($\pi_{0,+1}, \pi_{0,-1}$), the process of longitudinal relaxation of spin state $\rho(t)$

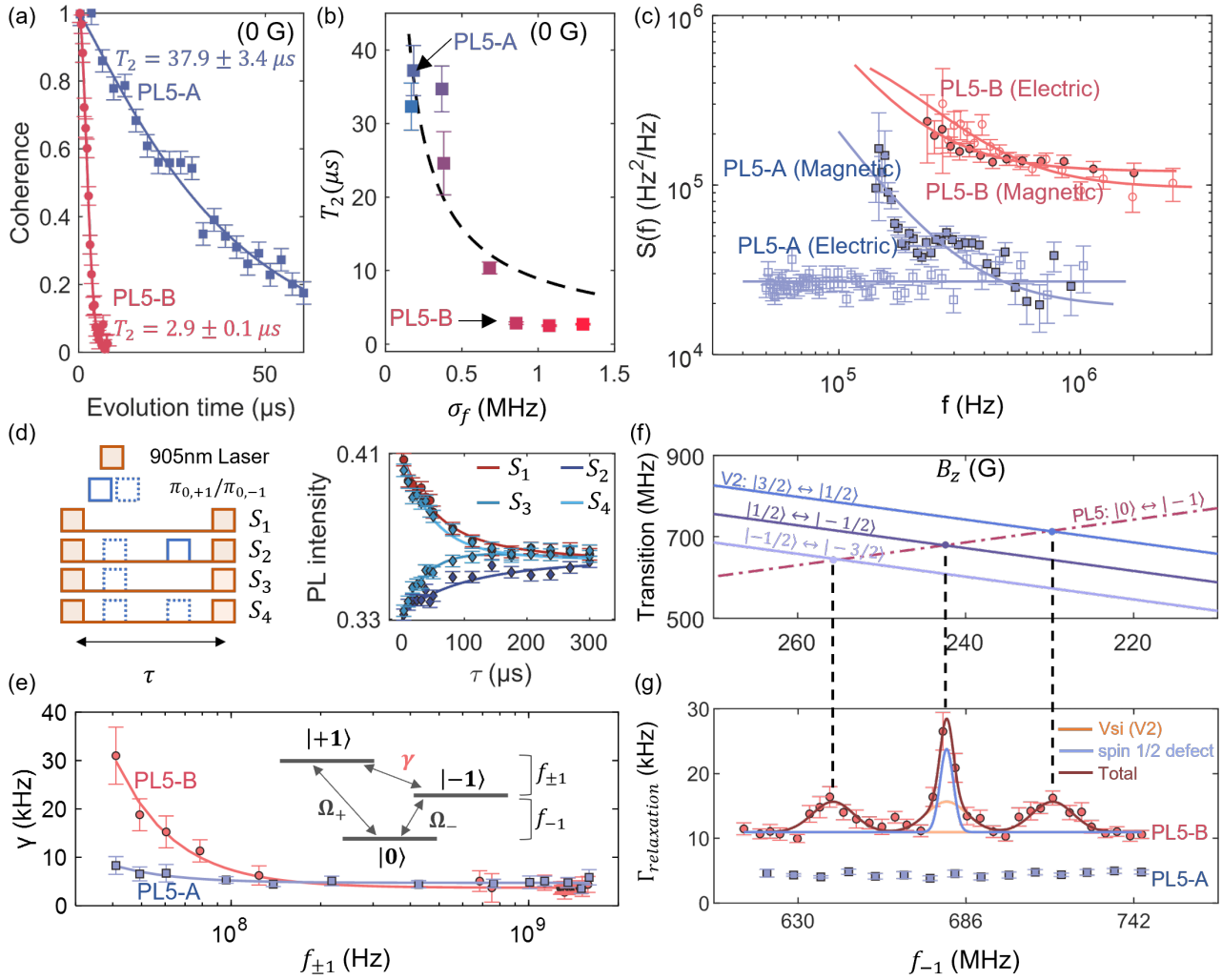


Fig.4. Noise strength correlation and spectrum of PL5 centers with EPR identification of noise source. (a) Hahn echo T_2 measurement of the two PL5 centers (named PL5-A and PL5-B) on wafer 1. The sensor with lower near-DC noise (PL5-A) exhibits a longer coherence time. (b) A rapid decrease in Hahn echo coherence time is observed as the spectral fluctuation (σ_f) increases, indicating a strong correlation between near-DC noise and high-frequency electrical noise. The dashed curve serves as a fitting guideline with $T_2 \propto 1/\sigma^k$. (c) Noise spectra obtained from XY8 dynamical decoupling measurements on PL5-A and PL5-B. Experiments were performed under both zero field and 120G magnetic field aligned along the defect axis. (d) SQ and DQ transition rates are extracted using different spin state initialization and readout schemes. Right pannel shows the measurement result of PL5-B at 260.4G along PL5 axis. Fitting model follows the equation shown in Eq.2. (e) Comparison of electrical noise strength γ between the two PL5 centers, showing that the unstable sensor exhibits a stronger $1/f$ -type noise. (f) Transition energy (Δ) for PL5 center and V2 center are plotted against magnetic field. (g) T_1 relaxometry for two PL5 centers. Here, relaxation rate Γ was extracted from $S_1 - S_3$ shown in (d). The observed accelerated relaxation of PL5-B reveals the presence of environmental noise. Based on the extracted spectral peak position and calculation of transition energy shown in (f), we attribute this signal to nearby silicon vacancy (V2) and other spin-1/2 traps, while no signal was observed for PL5-A. Errorbar is given by 1 SD.

can be described by rate equation

$$\dot{\rho}(t) = \Gamma \rho(t) \quad (2)$$

where the decay matrix is given by [31, 33]

$$\Gamma = \begin{pmatrix} -\Omega_{+1} - \gamma & \Omega_{+1} & \gamma \\ \Omega_{+1} & -\Omega_{+1} - \Omega_{-1} & \Omega_{-1} \\ \gamma & \Omega_{-1} & -\Omega_{-1} - \gamma \end{pmatrix} \quad (3)$$

Based on this method, we observed two important phenomena. First, in the tens-of-MHz regime of DQ transition rate measurements, we observed $1/f^\alpha$ -type electri-

cal noise in both PL5-A and PL5-B as shown in Figure 4(e). The PL5-B, which shows unstable ODMR positions in former experiment, exhibits stronger $1/f^\alpha$ noise compared to PL5-A. This confirms the presence of an ensemble of two-level fluctuators in the environment surrounding the unstable quantum sensor, which provide valuable insight into the characterization of the internal noise environment in semiconductors. Secondly, to analyze the type of noise source nearby, we examined its magnetic noise spectrum by varying the magnetic field and extracted relaxation rate Γ from $S_1 - S_3$ shown in Figure 4(d). The resulting spectra reveal a di-

rect causal link between specific defect species and charge noise. For PL5-B, we observed distinct resonance peaks at $g = 2.0$, accompanied by satellite features [Figure 4(f-g)], which can be attributed to relaxation enhancement between PL5-B and nearby traps. Data were fitted using a composite model comprising three Gaussian functions of equal amplitude and width, supplemented by an additional central Gaussian peak. Based on the fitting result ($f_1 = 229.7 \pm 0.8$, $f_2 = 242.3 \pm 0.1$, $f_3 = 255.9 \pm 0.8$ MHz) and theoretical calculation [Figure 4(f)], our results corresponds to a defect configuration consisting of silicon vacancies ($V_{Si}(V2)$, $2D = 70$ MHz) [34] while the distinct relaxation peak emerging in the middle provides a signature of other other spin-1/2 dark traps background (e.g. carbon vacancies V_C) as shown in Figure 4(g). In comparison, we observed no signal for the CW-stable quantum sensor PL5-A. When the B_z was scanned over a wide range from 20 - 300 G, the SQ and DQ transition rates remained unchanged, maintaining a ratio $\frac{\gamma}{\Omega} \approx 2.4$, where $\Omega \equiv \Omega_{+1} = \Omega_{-1}$ (see Supplementary Material [27]). This result demonstrates the capability of our method to perform spatially resolved chemical identification. By retrieving spectroscopic fingerprints from distinct locations, we can effectively resolve the specific defect composition within different nanoscopic regions of the sample, revealing the material's heterogeneity using single quantum sensor. Finally, our estimation of the magnetic sensing range ($5 \sim 8$ nm) shows a spatial consistency with the electrical noise measurements (shown in [27]). This finding points to a common origin for the electromagnetic fluctuations, further corroborating our identification of nearby traps as the dominant local noise source.

Conclusion. Our study demonstrates a robust, broadband quantum sensing protocol capable of diagnosing wafer-level quality variations with nanoscale precision by employing PL5 as noise sensors. Through systematic monitoring of these sensors, we reports the first real-time observation of single-charge tunneling dynamics in commercial semiconductor material at room temperature. Our findings deepen insight into the electrical landscape and defect engineering in SiC semiconductors and establish a room-temperature imaging approach for noise characterization, which functions as a quantitative metric for assessing wafer quality. Furthermore, our observation of the relation between spectral peak stability and coherence time suggests a correlation between noise sources at different frequencies level. Using dynamical decoupling and T_1 relaxation measurement, we provided the first nanoscale EPR spectroscopic fingerprint of charge defects in SiC. The observed spectral features indicate the existence of nearby silicon vacancies ($V2$) and other spin 1/2 defects (e.g., carbon vacancies), which also demonstrates the dipole-dipole interactions among distinct qubit species (PL5 and $V2$) within the SiC platform. Given that $V2$ and PL5 centers possess

distinct excitation and emission bands [35, 36], this finding highlights the promising prospect of realizing scalable hybrid qubits utilizing heterogeneous spin systems in the same material platform.

From the perspective of qubit optimization, our results underscore the pivotal role of substrate-hosted charge defects in driving solid-state qubit decoherence, thereby highlighting the necessity of high-quality substrates for realizing high-performance qubits. Crucially, this work establishes the solid-state spin as a versatile broadband quantum sensor, uniquely capable of characterizing wafer quality with nanoscale sensitivity and providing precise spectroscopic identification of local charge defects.

From the fabrication perspective, employing low-energy ion implantation allows for the creation of ultra-shallow sensors near the surface [37]. Combined with SiC's superior surface passivation and the non-invasive nature of near-infrared excitation which avoids photo-carrier generation in narrow-bandgap samples, our approach may overcome key limitations of diamond NV centers (532 nm excitation), which often suffer from surface charge screening when sensing external electric fields [15]. We envision transforming commercial SiC wafers into smart quantum substrates or scanning probes capable of universal diagnostics. This native platform enables the in-operando monitoring of diverse environments, ranging from ferroelectric vortices in epitaxially grown van der Waals heterostructures [38] to critical interface Coulomb scattering in SiC-CMOS devices [39].

Our approach can be generalized to other defect species in SiC and wide-field imaging can be incorporated in practical measurement to increase speed and field of view [13]. We believe our method will serve as a vital tool for the precise characterization of third-generation semiconductors, paving the way for high-throughput, atomic-scale defect engineering and spin-spin interfaces of qubits implemented in silicon carbide for quantum information and sensing applications.

This work was supported by the National Natural Science Foundation of China (Grant Nos. T2125011, 12174377), the CAS (Grant Nos. YSBR-068), Innovation Program for Quantum Science and Technology (Grant Nos. 2021ZD0302200, 2021ZD0303204, 2023ZD0300100), New Cornerstone Science Foundation through the XPLOTER PRIZE, “Pioneer” and “Leading Goose” R&D Program of Zhejiang (2025C01041) and the Fundamental Research Funds for the Central Universities (226-2024-00142). This work was partially carried out at the USTC Center for Micro and Nanoscale Research and Fabrication.

* These authors contributed equally to this work.

† zhq2011@ustc.edu.cn

✉ fzshi@ustc.edu.cn

[1] X. She, A. Q. Huang, O. Lucia, and B. Ozpineci, Review of Silicon Carbide Power Devices and Their Applications, *IEEE Transactions on Industrial Electronics* **64**, 8193 (2017).

[2] P.-C. Chen, W.-C. Miao, T. Ahmed, Y.-Y. Pan, C.-L. Lin, S.-C. Chen, H.-C. Kuo, B.-Y. Tsui, and D.-H. Lien, Defect Inspection Techniques in SiC, *Nanoscale Research Letters* **17**, 30 (2022).

[3] M. E. Bathen, C. T.-K. Lew, J. Woerle, C. Dorfer, U. Grossner, S. Castelletto, and B. C. Johnson, Characterization methods for defects and devices in silicon carbide, *Journal of Applied Physics* **131**, 140903 (2022).

[4] F. Dolde, M. W. Doherty, J. Michl, I. Jakobi, B. Naydenov, S. Pezzagna, J. Meijer, P. Neumann, F. Jelezko, N. B. Manson, and J. Wrachtrup, Nanoscale Detection of a Single Fundamental Charge in Ambient Conditions Using the NV - Center in Diamond, *Physical Review Letters* **112**, 097603 (2014).

[5] F. Dolde, H. Fedder, M. W. Doherty, T. Nöbauer, F. Rempp, G. Balasubramanian, T. Wolf, F. Reinhard, L. C. L. Hollenberg, F. Jelezko, and J. Wrachtrup, Electric-field sensing using single diamond spins, *Nature Physics* **7**, 459 (2011).

[6] H. Jayakumar, J. Henshaw, S. Dhomkar, D. Pagliero, A. Laraoui, N. B. Manson, R. Albu, M. W. Doherty, and C. A. Meriles, Optical patterning of trapped charge in nitrogen-doped diamond, *Nature Communications* **7**, 12660 (2016).

[7] A. Lozovoi, H. Jayakumar, D. Daw, G. Vizkelethy, E. Bielejec, M. W. Doherty, J. Flick, and C. A. Meriles, Optical activation and detection of charge transport between individual colour centres in diamond, *Nature Electronics* **4**, 717 (2021).

[8] A. A. Wood, D. J. McCloskey, N. Dotschuk, A. Lozovoi, R. M. Goldblatt, T. Delord, D. A. Broadway, J.-P. Tetienne, B. C. Johnson, K. T. Mitchell, C. T.-K. Lew, C. A. Meriles, and A. M. Martin, 3D-Mapping and Manipulation of Photocurrent in an Optoelectronic Diamond Device, *Advanced Materials* , 2405338 (2024).

[9] T. Delord, R. Monge, and C. A. Meriles, Correlated Spectroscopy of Electric Noise with Color Center Clusters, *Nano Letters* **24**, 6474 (2024).

[10] W. Ji, Z. Liu, Y. Guo, Z. Hu, J. Zhou, S. Dai, Y. Chen, P. Yu, M. Wang, K. Xia, F. Shi, Y. Wang, and J. Du, Correlated sensing with a solid-state quantum multisensor system for atomic-scale structural analysis, *Nature Photonics* **18**, 230 (2024).

[11] C. F. Weng, S. R. Lin, J. X. Zhao, Y. J. Yang, M. Y. Cai, Y. H. Guo, L. R. Lou, W. Zhu, and G. Z. Wang, Tracking single charge jumping with an individual color center in diamond, *Physical Review B* **109**, 224104 (2024).

[12] A. Lozovoi, G. Vizkelethy, E. Bielejec, and C. A. Meriles, Imaging dark charge emitters in diamond via carrier-to-photon conversion, *Science Advances* **8**, eabl9402 (2022).

[13] R. Monge, Y. Nakamura, O. Bach, J. Shao, A. Lozovoi, A. A. Wood, K. Sasaki, K. Kobayashi, T. Delord, and C. A. Meriles, Beyond ensemble averaging: Parallelized single-shot readout of hole capture in diamond (2025), arXiv:2507.11722 [cond-mat.mes-hall].

[14] J. Du, F. Shi, X. Kong, F. Jelezko, and J. Wrachtrup, Single-molecule scale magnetic resonance spectroscopy using quantum diamond sensors, *Reviews of Modern Physics* **96**, 025001 (2024).

[15] L. Oberg, M. De Vries, L. Hanlon, K. Strazzins, M. S. Barson, M. Doherty, and J. Wrachtrup, Solution to Electric Field Screening in Diamond Quantum Electrometers, *Physical Review Applied* **14**, 014085 (2020).

[16] C. L. Degen, F. Reinhard, and P. Cappellaro, Quantum sensing, *Rev. Mod. Phys.* **89**, 035002 (2017).

[17] C. P. Anderson, A. Bourassa, K. C. Miao, G. Wolfowicz, P. J. Mintun, A. L. Crook, H. Abe, J. Ul Hassan, N. T. Son, T. Ohshima, and D. D. Awschalom, Electrical and optical control of single spins integrated in scalable semiconductor devices, *Science* **366**, 1225 (2019).

[18] Z. Li, X. Guo, Y. Jin, F. Andreoli, A. Bilgin, D. D. Awschalom, N. Delegan, F. J. Heremans, D. Chang, G. Galli, and A. A. High, Atomic optical antennas in solids, *Nature Photonics* **10**, 1038/s41566-024-01456-5 (2024).

[19] G. Pieplow, C. G. Torun, C. Gurr, J. H. D. Munns, F. M. Herrmann, A. Thies, T. Pregnolato, and T. Schröder, Quantum electrometer for time-resolved material science at the atomic lattice scale, *Nature Communications* **16**, 6435 (2025).

[20] W. F. Koehl, B. B. Buckley, F. J. Heremans, G. Calusine, and D. D. Awschalom, Room temperature coherent control of defect spin qubits in silicon carbide, *Nature* **479**, 84 (2011).

[21] H. Hu, Y. Zhou, A. Yi, T. Bao, C. Liu, Q. Luo, Y. Zhang, Z. Wang, Q. Li, D. Lu, Z. Liu, S. Xiao, X. Ou, and Q. Song, Room-temperature waveguide integrated quantum register in a semiconductor photonic platform, *Nature Communications* **15**, 10256 (2024).

[22] Q. Li, J.-F. Wang, F.-F. Yan, J.-Y. Zhou, H.-F. Wang, H. Liu, L.-P. Guo, X. Zhou, A. Gali, Z.-H. Liu, Z.-Q. Wang, K. Sun, G.-P. Guo, J.-S. Tang, H. Li, L.-X. You, J.-S. Xu, C.-F. Li, and G.-C. Guo, Room-temperature coherent manipulation of single-spin qubits in silicon carbide with a high readout contrast, *National Science Review* **9**, nwab122 (2022).

[23] Y. Chen, Q. Zhang, M. Liu, J. Liu, J. Zhou, P. Yu, S. Lin, Y. Teng, W. Yu, Y. Wang, C. Duan, F. Shi, and J. Du, Atomic structure analysis of pl5 in silicon carbide with single-spin spectroscopy (2025), arXiv:2504.07558 [cond-mat.mtrl-sci].

[24] A. L. Falk, P. V. Klimov, B. B. Buckley, V. Ivády, I. A. Abrikosov, G. Calusine, W. F. Koehl, A. Gali, and D. D. Awschalom, Electrically and Mechanically Tunable Electron Spins in Silicon Carbide Color Centers, *Physical Review Letters* **112**, 187601 (2014).

[25] C. Zeledon, B. Pingault, J. C. Marcks, M. Onizhuk, Y. Tsaturyan, Y. xin Wang, B. S. Soloway, H. Abe, M. Ghezellou, J. Ul-Hassan, T. Ohshima, N. T. Son, F. J. Heremans, G. Galli, C. P. Anderson, and D. D. Awschalom, Minute-long quantum coherence enabled by electrical depletion of magnetic noise (2025), arXiv:2504.13164 [quant-ph].

[26] T. Steidl, P. Kuna, E. Hesselmeier-Hüttmann, D. Liu, R. Stöhr, W. Knolle, M. Ghezellou, J. Ul-Hassan, M. Schober, M. Bockstedte, G. Bian, A. Gali, V. Vorobyov, and J. Wrachtrup, Single V2 defect in 4H silicon carbide Schottky diode at low temperature, *Nature Communications* **16**, 10.1038/s41467-025-59647-9 (2025).

[27] See Supplemental Material at [url] for setup and sample information, CW-ODMR analysis, charge location calculation and other noise characterization results.

[28] J. F. Ziegler, M. Ziegler, and J. Biersack, SRIM – The stopping and range of ions in matter (2010), *Nuclear Instruments and Methods in Physics Research Section B: Beam Interactions with Materials and Atoms* **268**, 1818 (2010).

[29] Y.-K. Tzeng, P.-C. Tsai, H.-Y. Liu, O. Y. Chen, H. Hsu, F.-G. Yee, M.-S. Chang, and H.-C. Chang, Time-Resolved Luminescence Nanothermometry with Nitrogen-Vacancy Centers in Nanodiamonds, *Nano Letters* **15**, 3945 (2015).

[30] R. S. Schoenfeld and W. Harneit, Real Time Magnetic Field Sensing and Imaging Using a Single Spin in Diamond, *Physical Review Letters* **106**, 030802 (2011).

[31] B. A. Myers, A. Ariyaratne, and A. C. B. Jayich, Double-Quantum Spin-Relaxation Limits to Coherence of Near-Surface Nitrogen-Vacancy Centers, *Physical Review Letters* **118**, 197201 (2017).

[32] A. Gardill, M. Cambria, and S. Kolkowitz, Fast relaxation on qutrit transitions of nitrogen-vacancy centers in nanodiamonds, *Phys. Rev. Appl.* **13**, 034010 (2020).

[33] Z. Zhao, X. Ye, S. Xu, P. Yu, Z. Yang, X. Kong, Y. Wang, T. Xie, F. Shi, and J. Du, Sub-nanotesla sensitivity at the nanoscale with a single spin, *National Science Review* **10**, nwad100 (2023).

[34] V. Ivády, J. Davidsson, N. T. Son, T. Ohshima, I. A. Abrikosov, and A. Gali, Identification of Si-vacancy related room-temperature qubits in 4H silicon carbide, *Physical Review B* **96** (2017).

[35] S. Castelletto, C. T.-K. Lew, W.-X. Lin, and J.-S. Xu, Quantum systems in silicon carbide for sensing applications, *Rep. Prog. Phys.* (2024).

[36] H. Roberts, H. Abudayyeh, X. Li, and X. Li, Quantum Sensing with Spin Defects Beyond Diamond, *ACS Nano* **19**, 22528 (2025).

[37] P. Li, J.-Y. Zhou, S. Li, P. Udvarhelyi, J.-S. Xu, C.-F. Li, B. Huang, G.-C. Guo, and A. Gali, Non-invasive bioinert room-temperature quantum sensor from silicon carbide qubits, *Nature Materials* **24**, 1913 (2025).

[38] C. Wang, L. You, D. Cobden, and J. Wang, Towards two-dimensional van der Waals ferroelectrics, *Nature Materials* **22**, 542 (2023).

[39] K. Naydenov, N. Donato, and F. Udrea, An advanced physical model for the Coulombic scattering mobility in 4H-SiC inversion layers, *Journal of Applied Physics* **127**, 194504 (2020).